Experimental observation of repulsively bound magnons

Zhe Wang[1,2,3]✉, Catalin-Mihai Halati[4,5], Jean-Sébastien Bernier[5,6], Alexey Ponomaryov[7,8], Denis I. Gorbunov[7], Sandra Niesen[2], Oliver Breunig[2], J. Michael Klopf[8], Sergei Zvyagin[7], Thomas Lorenz[2], Alois Loidl[3] & Corinna Kollath[5]

Stable composite objects, such as hadrons, nuclei, atoms, molecules and superconducting pairs, formed by attractive forces are ubiquitous in nature. By contrast, composite objects stabilized by means of repulsive forces were long thought to be theoretical constructions owing to their fragility in naturally occurring systems. Surprisingly, the formation of bound atom pairs by strong repulsive interactions has been demonstrated experimentally in optical lattices[1]. Despite this success, repulsively bound particle pairs were believed to have no analogue in condensed matter owing to strong decay channels. Here we present spectroscopic signatures of repulsively bound three-magnon states and bound magnon pairs in the Ising-like chain antiferromagnet $BaCo_2V_2O_8$. In large transverse fields, below the quantum critical point, we identify repulsively bound magnon states by comparing terahertz spectroscopy measurements to theoretical results for the Heisenberg–Ising chain antiferromagnet, a paradigmatic quantum many-body model[2–5]. Our experimental results show that these high-energy, repulsively bound magnon states are well separated from continua, exhibit notable dynamical responses and, despite dissipation, are sufficiently long-lived to be identified. As the transport properties in spin chains can be altered by magnon bound states, we envision that such states could serve as resources for magnonics-based quantum information processing technologies[6–8].

The stability of attractively bound pairs is typically rooted in their binding forces lowering the energy of the state. For example, in ferromagnets, spin waves whose quantization corresponds to a bosonic quasiparticle, a magnon, are the conventional excitations. There, because of the attractive ferromagnetic interaction, two magnon excitations can remain bound together, forming a two-magnon attractively bound state[9–11]. By contrast, the formation of stable composite objects owing to repulsive interaction typically increases the system energy. For cold bosonic atoms in optical lattices, repulsively bound on-site pairs dressed with quantum fluctuations become stable eigenstates when the on-site repulsive interaction between atoms is much larger than the tunnelling rate. As these atoms are only weakly coupled to dissipative channels, such bound objects have been observed to move through the lattice as dressed pairs for relatively long times because their large repulsion energy cannot be converted into kinetic energy[1,12].

Whereas many condensed-matter systems host attractively bound pairs, the realization of repulsively bound states in solid-state materials, in the absence of further symmetry protection, has been considered impossible because of several relaxation channels. Here we overcome this challenge by carefully choosing the compound to optimize the stability of these states. We report on the experimental signatures of repulsively bound two-magnon and three-magnon states in the antiferromagnetic compound $BaCo_2V_2O_8$ modelled, under a strong transverse magnetic field, as a Heisenberg–Ising spin-1/2 chain.

$BaCo_2V_2O_8$ is exceptionally suited for the observation of repulsively bound states owing to several properties[13–15]: (1) nearest-neighbouring spins are antiferromagnetically coupled[13,14], leading to a repulsive interaction between magnons; (2) the transverse-field-induced transition to the polarized phase is experimentally within reach[15]; (3) owing to the material crystallographic structure, the spins are subjected to an effective staggered magnetic field as well as a uniform component[13,14]; (4) with increasing field, the one-dimensionality becomes more pronounced, effectively enhancing its strongly correlated nature[15].

This last point is particularly crucial as this compound is described by the standard transverse-field Heisenberg–Ising spin-1/2 chain model. This model is of high importance for understanding a variety of physical phenomena, including quantum criticality and duality[3–5], topological excitations[16,17] and quench dynamics[18–21], and has greatly affected various branches of physics, ranging from condensed matter and cold atoms to quantum information. Here we show that this model has yet to reveal some of its secrets, as we demonstrate that it can even host two-magnon and three-magnon repulsively bound states.

[1]Department of Physics, TU Dortmund University, Dortmund, Germany. [2]Institute of Physics II, University of Cologne, Cologne, Germany. [3]Experimental Physics V, Center for Electronic Correlations and Magnetism, Institute of Physics, University of Augsburg, Augsburg, Germany. [4]Department of Quantum Matter Physics, University of Geneva, Geneva, Switzerland. [5]Physikalisches Institut, University of Bonn, Bonn, Germany. [6]Department of Physics, University of Northern British Columbia, Prince George, British Columbia, Canada. [7]Dresden High Magnetic Field Laboratory (HLD-EMFL), Helmholtz-Zentrum Dresden-Rossendorf (HZDR), Dresden, Germany. [8]Institute of Radiation Physics, Helmholtz-Zentrum Dresden-Rossendorf (HZDR), Dresden, Germany. ✉e-mail: zhe.wang@tu-dortmund.de

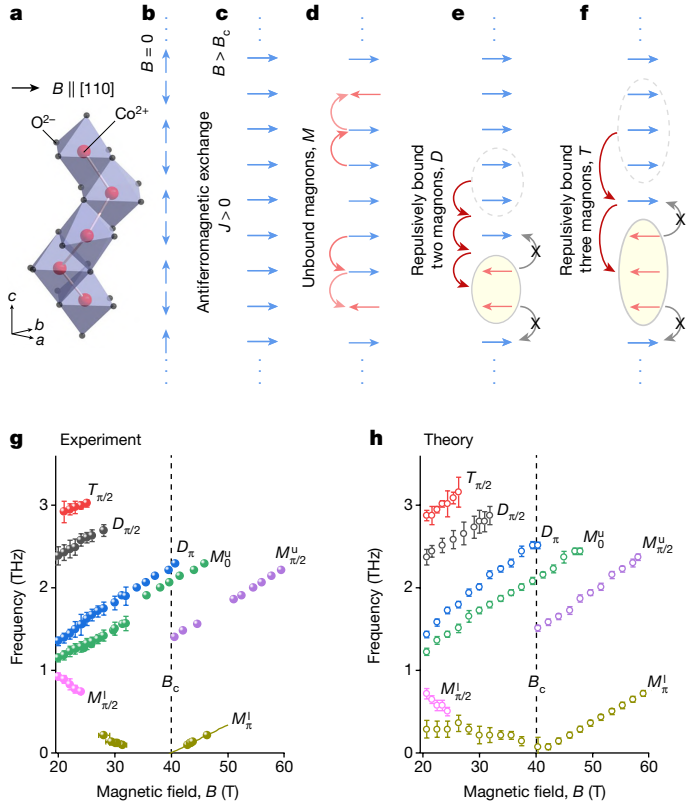

Fig. 1 | Repulsively bound two and three magnons for a Heisenberg–Ising antiferromagnetic chain in a strong transverse field. a, A fourfold screw chain of spin-1/2 Co^{2+} ions in $BaCo_2V_2O_8$. **b**, Antiferromagnetic ground state in zero field corresponding to antiparallel alignment of spins with Ising easy axis in the crystallographic *c* direction. **c**, Fully field-polarized state above the one-dimensional transverse-field Ising quantum critical point, $B > B_c$. **d**, States of two unbound magnons corresponding to two spin flips (red arrows), which are well separated and propagate independently in the chain (curved red arrows). **e**, Sketch of repulsively bound two-magnon states, with the two spin flips occupying adjacent sites. **f**, Sketch of repulsively bound three-magnon states, with the three spin flips occupying adjacent sites. The bound magnons do not propagate separately (curved grey arrows) but as an entity (curved red arrows) along the chain. **g**,**h**, Eigenfrequencies as a function of transverse field for all of the experimentally observed magnetic excitations (**g**) and for the corresponding modes obtained by the numerically exact time-dependent matrix product state algorithm using the parameters $J = 2.82$ meV, $\Delta = 1.92$, $g_u^x = 3.06$, $g_s^x = 0.66$ and $g^z = 0.21$ (**h**). Very good agreement between experiment and theory is achieved. Above $B_c = 40$ T, the single-magnon modes (M^l_π, $M^u_{\pi/2}$ and M^u_0 at the quasi-momenta $q = \pi$, $\pi/2$ and 0, respectively; see Fig. 4) are observed in the field-polarized phase. The solid line in **g** is a linear fit of the low-lying M^l_π mode, which determines the critical field of $B_c = 40$ T. Below B_c, excitations of the repulsively bound three magnons ($T_{\pi/2}$ at $q = \pi/2$), two magnons ($D_{\pi/2}$ and D_π at $q = \pi/2$ and $q = \pi$, respectively), as well as the single magnons ($M^l_{\pi/2}$ and M^l_π at $q = \pi/2$ and $q = \pi$, respectively) are identified by their field-dependent eigenenergies. Experimental and theoretical linewidths are indicated by bars.

A simplified sketch of two-magnon and three-magnon bound states above the spin-polarized ground state (Fig. 1c) realized by the application of a strong magnetic field is presented in Fig. 1e,f. Owing to the presence of an antiferromagnetic exchange coupling, the energy of two neighbouring magnons (Fig. 1e) is higher than the energy of two unbound spatially distant ones (Fig. 1d). In $BaCo_2V_2O_8$, the energy difference between the bound and unbound states is further increased by the presence of a spatially dependent effective magnetic field, a crucial ingredient for their experimental observation. Figure 1e,f only depicts a simplified classical representation of magnons and quantum bound states, neglecting their dressing by quantum fluctuations.

In Fig. 1g, the experimentally detected modes are represented by their frequencies versus applied transverse field. Comparing with a one-dimensional Heisenberg–Ising (or XXZ) model, we demonstrate that the observed higher-energy modes marked by *D* and *T* are associated with two-magnon and three-magnon repulsively bound states, respectively. In the experimentally accessed low-temperature and high-field regime, the long-range magnetic order stabilized owing to small interchain couplings has been suppressed[15]. Hence we neglect small interchain couplings present in real materials and describe each spin chain by the one-dimensional XXZ spin-1/2 model

$$H = J\sum_{j=1}^{L-1}\left(S_j^x S_{j+1}^x + S_j^y S_{j+1}^y + \Delta S_j^z S_{j+1}^z\right) - \mu_B B_x \sum_{j=1}^{L}\left(g_j^{xx} S_j^x + g_j^{xz} S_j^z\right), \quad (1)$$

with an antiferromagnetic exchange, $J > 0$, and an Ising-like anisotropy, $\Delta > 1$ (refs. 13,14,22,23). $S_j^{x,y,z}$ denote the spin components at the *j*th site of the chain with length *L*. The *x* coordinate is defined parallel to the applied field B_x along [110], whereas *y* and *z* are along the [−110] and *c* directions, respectively. The last term describes the Zeeman interaction, given the Landé *g*-factors g_j^{xx} and g_j^{xz} and the Bohr magneton μ_B. The anisotropic *g*-values result from the edge-sharing CoO_6 octahedra[13,14], which form a fourfold screw chain along the *c* direction (Fig. 1a).

In this isolated chain model, the positive exchange *J* induces an antiferromagnetic ground state at zero field (Fig. 1b). In this regime, the elementary excitations are spinons[24–28] carrying a fractional quantum number of spin-1/2. In the applied transverse field, a phase transition into a quantum paramagnetic phase occurs at a critical field B_c. This state is characterized by a field-induced polarization of the spins (Fig. 1c). According to measurements of magnetization, sound velocity and magnetocaloric effect[15], the quantum phase transition of a transverse-field Ising nature[3,29] occurs in $BaCo_2V_2O_8$ at $B_c = 40$ T. Above the polarized ground state, the low-energy excitations are magnons and, because of quantum fluctuations, a finite density of spin flips is already present in this ground state. Because the magnetization in the field direction is important at large fields even below B_c, the excitations in the regime $0 \ll B < B_c$ can be described in terms of magnons[30].

In this work, we address the following fundamental question: can repulsively bound states of two or three magnons be formed when the strongly fluctuating ground state is perturbed by a photon or neutron flipping an extra spin? For strong transverse fields, as the effective interaction between magnons is repulsive, that is, $\propto J > 0$, the energy of such magnon bound states would be larger than that of unbound magnons. In principle, many such high-energy states should exist. However, to be sufficiently stable and detectable, these states need to be well separated from excitation continua. This condition is fulfilled in $BaCo_2V_2O_8$, in which staggered magnetic-field components are induced by the site-dependent *g*-factors, $g_j^{xx} = g_u^x - (-1)^j g_s^x$ and $g_j^{xz} = g^z \sin\left(\frac{\pi}{2} j\right)$ (see Methods).

Quantum spin dynamics around B_c

We present below our experimental results highlighting the presence of repulsively bound magnon states in $BaCo_2V_2O_8$. This compound is excited with a magnetic field of terahertz photons (1 THz ≈ 4.1 meV) in applied pulsed fields up to 61 T. The obtained absorption spectra are shown in Fig. 2a. At 1.478 THz, the spectrum exhibits one resonance peak (labelled $M^u_{\pi/2}$) above B_c at 42.1 T and two further peaks at 29.8 T and 22.8 T below B_c, labelled as M^u_0 and D_π, respectively. All three modes shift to higher fields with increasing frequencies. The $M^u_{\pi/2}$ mode is sharply resolved above B_c, whereas at low fields, it is barely traceable. By contrast, the other two modes (M^u_0 and D_π) can still be clearly

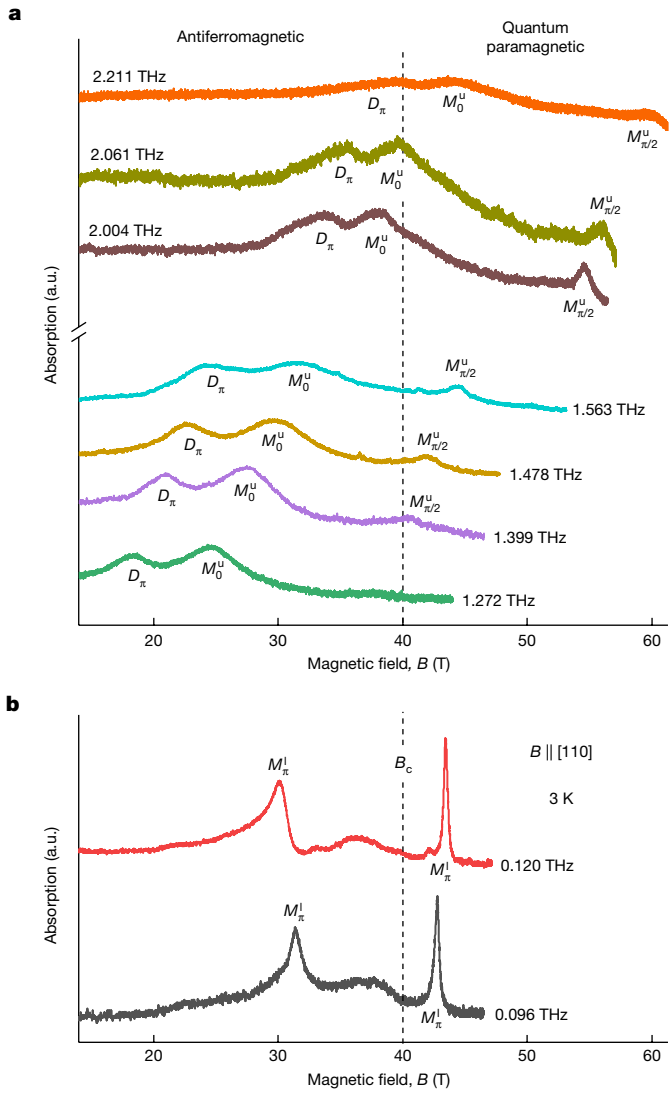

Fig. 2 | Quantum spin dynamics around the one-dimensional transverse-field Ising quantum critical point. a, Absorption spectra at various frequencies exhibit resonance peaks corresponding to the higher-energy excitations D_π, M^u_0 and $M^u_{\pi/2}$. **b**, Field-dependent evolution of the lowest-lying mode M^l_π indicates the gap closing and reopening in the vicinity of the quantum phase transition at $B_c = 40$ T, which belongs to the one-dimensional transverse-field Ising universality class[15]. Above B_c, the system enters a fully field-polarized quantum paramagnetic phase (see Fig. 1c for an illustration). The spectra of higher frequencies are shifted upwards for clarity. a.u., arbitrary units.

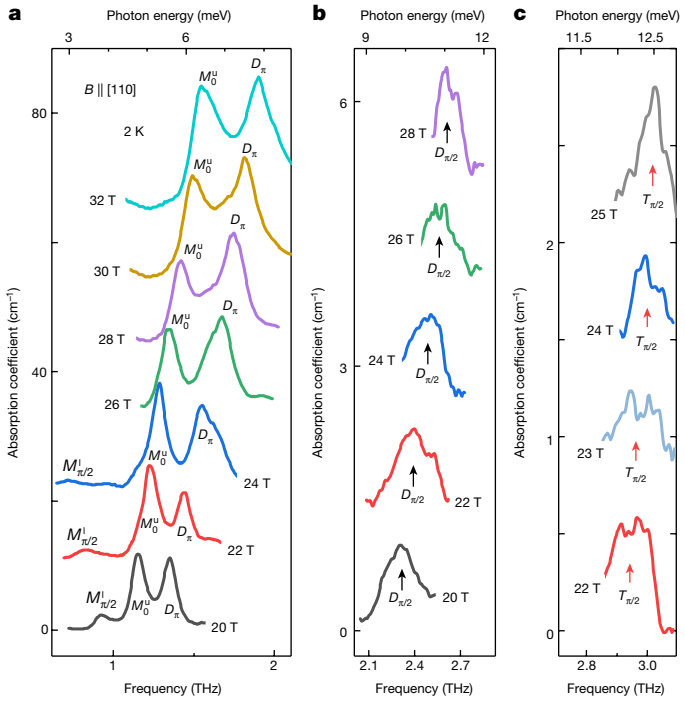

Fig. 3 | New types of high-energy excitation in the regime $0 \ll B < B_c$. a, Three different excitations M^u_0, D_π and $M^l_{\pi/2}$ are observed, each with a different characteristic field dependence. **b**,**c**, Higher-energy modes $D_{\pi/2}$ (**b**) and $T_{\pi/2}$ (**c**) with smaller absorption coefficient, as indicated by the arrows, are resolved in high fields below B_c (see also Extended Data Fig. 5). Although the $M^l_{\pi/2}$ mode softens, the eigenenergies of the other modes increase with increasing fields. The spectra in higher fields are shifted upwards for clarity.

detected at lower fields. At much lower frequencies, such as for 0.120 THz (Fig. 2b), our electron-spin-resonance spectroscopy reveals two resonance peaks above and below B_c at 30.1 T and 43.4 T, respectively. By decreasing the frequency, we observe both peaks approaching the critical field, an indication of gap closure at B_c.

Quantum spin dynamics at $0 \ll B < B_c$

We explore the quantum spin dynamics at even higher energies by carrying out magneto-optic measurements in strong static magnetic fields up to 32 T. As shown in Fig. 3a, the absorption spectra at 2 K and 32 T is characterized by two peaks at 1.56 THz and 1.90 THz, precisely corresponding to the resonance modes M^u_0 and D_π, revealed by the field-sweeping electron-spin-resonance technique (Fig. 2a). The modes M^u_0 and D_π soften as the field is decreased. By contrast, at 24 T, another lower-frequency mode $M^l_{\pi/2}$ appears, with substantially smaller spectral weight, which evolves towards higher frequencies at lower fields. In the highest available frequency range above 2 THz (whose photon energy is >3J), we resolve two further modes in the spectra (Fig. 3b,c). For example at 22 T, the mode $D_{\pi/2}$ is found at 2.47 THz and the mode $T_{\pi/2}$ at 2.92 THz. We can unambiguously resolve these two modes by their systematic shifts in the applied fields, even though they are characterized by a relatively small spectral weight.

Many-body numerical simulations

The experimental resonance frequencies versus magnetic fields are extracted for all of these excitations and summarized in Fig. 1g. We identify the nature of these modes by comparing them with our precise theoretical results (Fig. 1h). The theoretical modes are obtained by computing the dynamical spin structure factor $\mathcal{S}(q, \omega)$ (see Methods for the definition) describing the response to a single spin flip triggered by a linear coupling to the terahertz magnetic field and obeying the selection rule $\Delta S = \pm 1$. Owing to the fourfold screw symmetry (Fig. 1a), the zero-momentum transfer in the reduced zone scheme, examined by terahertz spectroscopy, corresponds to quasi-momenta 0, π/2 and π in the extended Brillouin zone. The dynamical structure factor is derived from many-body numerical simulations of the quantum spin dynamics for the Hamiltonian in equation (1) using the numerically exact time-dependent matrix product state algorithm[31–33]. Our results are presented in Fig. 4a–c for the three regimes $0 \ll B < B_c$, $B \approx B_c$ and $B > B_c$, respectively. Corresponding to the intensity maxima (as marked by green circles at the quasi-momenta $q = 0$, π/2 and π in Fig. 4), the frequencies extracted from the theoretical spectral function are shown in Fig. 1h for the comparison with the experimentally observed modes.

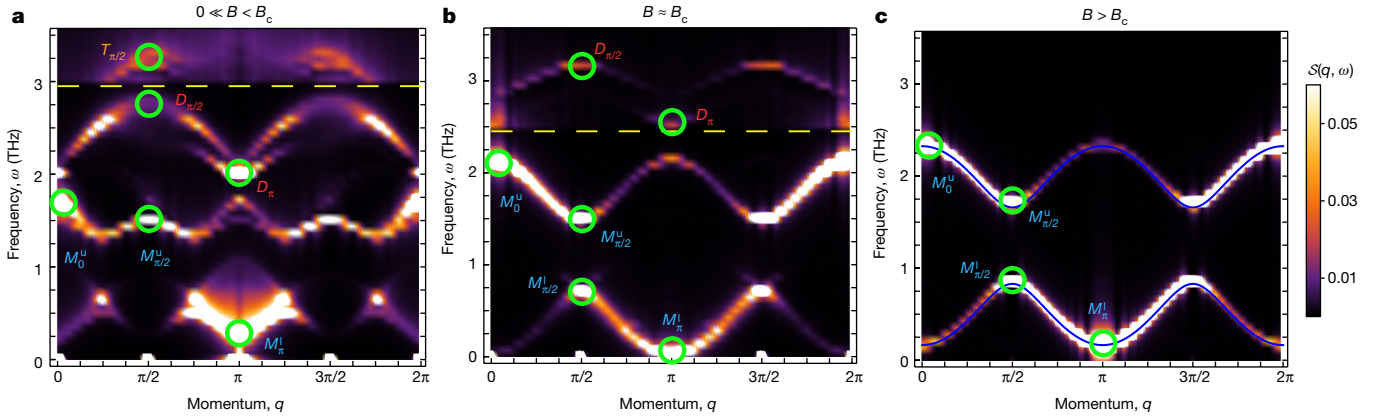

Fig. 4 | Characteristic quantum spin dynamics. a–c, Dynamical spin structure factor $\mathcal{S}(q,\omega)$ as a function of momentum q and frequency ω for an applied magnetic field $0 \ll B = 30\ \mathrm{T} < B_c$ (**a**), $B = 40.3\ \mathrm{T} \approx B_c$ (**b**) and $B = 45\ \mathrm{T} > B_c$ (**c**) using the numerically exact time-dependent matrix product state algorithm[31–33] for the transverse-field Heisenberg–Ising model in equation (1). The green circles mark the modes at the quasi-momenta $q = 0$, π/2 and π in the extended Brillouin zone, which correspond to zero-momentum transfer in the reduced zone scheme owing to the fourfold screw symmetry in the spin-chain structure (see Fig. 1a) and is experimentally detectable by terahertz spectroscopy. M, D and T denote the excitations of unbound magnons, repulsively bound two magnons and repulsively bound three magnons, respectively. In the corresponding labels, the subscript denotes the momentum q. In each panel, we normalized $\mathcal{S}(q,\omega)$ to its maximum value. To highlight the high-frequency modes above the horizontal dashed lines, we multiplied $\mathcal{S}(q,\omega)$ by a factor of 10. The blue curves in **c** depict the one-magnon dispersion computed analytically[30].

Comparison between experiment and theory

Very good agreement is achieved for all seven detected modes, using the parameters $J = 2.82$ meV, $\Delta = 1.92$, $g_u^x = 3.06$, $g_s^x = 0.66$ and $g^z = 0.21$. These values also provide an excellent description for the field-dependent magnetization (Extended Data Fig. 1) and are consistent with previously reported values[13–16,34–40] (Extended Data Tables 1 and 2). We find that, well above the critical field ($B \gg B_c$), the spins are polarized by the magnetic field (Fig. 1c). In this regime, the spin dynamics is characterized by unbound magnon excitations (see Fig. 4c and the sketch in Fig. 1d). However, instead of a single band, we obtain two distinct excitation bands, as denoted by M^l and M^u in Fig. 4c. The gap between the two bands is because of the site-dependent, staggered effective field, that is, $(-1)^j g_s^x B_x$ (Extended Data Fig. 2). Both bands correspond to unbound magnons, excited by the terahertz field, propagating along the chain.

With decreasing field towards B_c, both magnon bands shift to lower energies, as seen experimentally and theoretically. The lower mode marked by M_π^l decreases approximately linearly and becomes gapless at B_c, signalling the quantum phase transition. The gap of this mode reopens more slowly below B_c. A linear extrapolation of the field dependence above the B_c determines a critical field of $B_c = 40$ T (see Fig. 1g), in excellent agreement with thermodynamic measurements[15].

Close to the critical field, $B \approx B_c$, we identify new excitations (denoted by D in Fig. 4b) at energies higher than the unbound magnon bands. The characteristic energies of the D modes are not simply twice that of the M^l mode or of the M^u mode. To analyse the nature of the excitations, we monitor theoretically the expectation distance between the flipped spins present in the states contributing most to this dynamical-structure-factor feature[30]. As in a bound state, the magnons should mostly be confined next to each other and the distance should be small[30] (for example, <2.5 sites; see Fig. 1e), whereas for unbound magnons, the distance is usually much larger (Fig. 1d). Thereby, we identify the high-energy band D as being the excitation of repulsively bound two-magnon states[30]. For fields below B_c but still very large (for example, $B = 30$ T), we obtain an excitation band at even higher energy, as denoted by T above the dashed line in Fig. 4a. This band involves three flipped spins bound next to each other, with the average distance between the first and third spins being very small[30] (that is, <3.5 sites; see Fig. 1f). Thus, this band corresponds to the excitations of repulsively bound three magnons.

Identification of repulsively bound magnons

The very good agreement between experiment and theory enables the unambiguous identification of experimentally observed repulsively bound magnon states (see Fig. 1g,h). D_π and $D_{\pi/2}$ correspond to the excitations of repulsively bound two-magnon pairs and $T_{\pi/2}$ to the repulsively bound three-magnon states. The $D_{\pi/2}$ and D_π modes are at the maximum and minimum of the excitation band at the quasi-momenta $q = \pi/2$ and $q = \pi$, respectively (marked by green circles in Fig. 4a,b). However, the spectral weight corresponding to the repulsively bound three-magnon state is mostly concentrated around $q = \pi/2$ (Fig. 4a).

The experimental observation of the repulsively bound magnon states highlights their important role in one-dimensional quantum many-body spin dynamics. These peculiar states appear as high-energy many-body dynamical features in a regime characterized by strong one-dimensional spin fluctuations, $0 \ll B < B_c$, in which the antiferromagnetic exchange and the Zeeman interaction compete. The contribution of the repulsively bound magnons to the dynamics is enhanced by the staggered effective field (Extended Data Figs. 3 and 4), a distinctive feature of $BaCo_2V_2O_8$ facilitating their experimental observation. Above the critical field, quantum fluctuations are strongly suppressed and the spin dynamics is dominated by low-lying single-magnon excitations. There the dynamical response of the magnon bound states is negligibly small and experimentally undetectable.

The characteristic lifetime of the repulsively bound states can be estimated from the experimentally resolved linewidth (Fig. 3), which yields a typical value of 8 ± 2 ps. This is sufficiently long in comparison with their relatively high characteristic frequencies ($\omega > 1.2$ THz; see Fig. 3), allowing their experimental identification even in the presence of dissipation. Such high frequencies correspond to the strong exchange interactions, ensuring that the observed spin dynamics is governed by one-dimensional many-body quantum-mechanical effects rather than dissipation or thermal fluctuations. At elevated temperatures, thermally enhanced fluctuations (for example, lattice vibrations and spin fluctuations) will substantially reduce the lifetime of the repulsively bound magnons corresponding to broadened excitation lineshapes.

In conclusion, we demonstrate the existence of repulsively bound two-magnon and three-magnon states in a solid-state compound, beyond the realm of ultracold atoms in optical lattices[1,12], although thermal fluctuations and dissipative channels are present, as well as strong quantum fluctuations. These unconventional repulsively

bound states, together with their transport properties, are of particular interest in the fields of quantum communication, manipulation and sensing[6–8]. Our results also motivate comprehensive studies of exotic high-energy magnon dynamics in quantum magnets and of general composite excitations in complex many-body systems.

Online content

Any methods, additional references, Nature Portfolio reporting summaries, source data, extended data, supplementary information, acknowledgements, peer review information; details of author contributions and competing interests; and statements of data and code availability are available at https://doi.org/10.1038/s41586-024-07599-3.

1. Winkler, K. et al. Repulsively bound atom pairs in an optical lattice. *Nature* **441**, 853–856 (2006).
2. Pfeuty, P. The one-dimensional Ising model with a transverse field. *Ann. Phys.* **57**, 79–90 (1970).
3. Sachdev, S. *Quantum Phase Transitions* (Cambridge Univ. Press, 2011).
4. Dutta, A. et al. *Quantum Phase Transitions in Transverse Field Spin Models: From Statistical Physics to Quantum Information* (Cambridge Univ. Press, 2015).
5. Mussardo, G. *Statistical Field Theory: An Introduction to Exactly Solved Models in Statistical Physics* (Oxford Univ. Press, 2020).
6. Subrahmanyam, V. Entanglement dynamics and quantum-state transport in spin chains. *Phys. Rev. A* **69**, 034304 (2004).
7. Barman, A. et al. The 2021 magnonics roadmap. *J. Phys. Condens. Matter* **33**, 413001 (2021).
8. Yuan, H., Cao, Y., Kamra, A., Duine, R. A. & Yan, P. Quantum magnonics: when magnon spintronics meets quantum information science. *Phys. Rep.* **965**, 1–74 (2022).
9. Bethe, H. Zur Theorie der Metalle. I. Eigenwerte und Eigenfunktionen der linearen Atomkette. *Z. Phys.* **71**, 205–226 (1931).
10. Wortis, M. Bound states of two spin waves in the Heisenberg ferromagnet. *Phys. Rev.* **132**, 85–97 (1963).
11. Hanus, J. Bound states in the Heisenberg ferromagnet. *Phys. Rev. Lett.* **11**, 336–338 (1963).
12. Deuchert, A., Sakmann, K., Streltsov, A. I., Alon, O. E. & Cederbaum, L. S. Dynamics and symmetries of a repulsively bound atom pair in an infinite optical lattice. *Phys. Rev. A* **86**, 013618 (2012).
13. Kimura, S. et al. Collapse of magnetic order of the quasi one-dimensional Ising-like antiferromagnet $BaCo_2V_2O_8$ in transverse fields. *J. Phys. Soc. Jpn* **82**, 033706 (2013).
14. Niesen, S. K. et al. Magnetic phase diagrams, domain switching, and quantum phase transition of the quasi-one-dimensional Ising-like antiferromagnet $BaCo_2V_2O_8$. *Phys. Rev. B* **87**, 224413 (2013).
15. Wang, Z. et al. Quantum criticality of an Ising-like spin-1/2 antiferromagnetic chain in a transverse magnetic field. *Phys. Rev. Lett.* **120**, 207205 (2018).
16. Faure, Q. et al. Topological quantum phase transition in the Ising-like antiferromagnetic spin chain $BaCo_2V_2O_8$. *Nat. Phys.* **14**, 716–722 (2018).
17. Takayoshi, S., Furuya, S. C. & Giamarchi, T. Topological transition between competing orders in quantum spin chains. *Phys. Rev. B* **98**, 184429 (2018).
18. Calabrese, P., Essler, F. H. L. & Fagotti, M. Quantum quench in the transverse-field Ising chain. *Phys. Rev. Lett.* **106**, 227203 (2011).
19. Caux, J.-S. The quench action. *J. Stat. Mech. Theory Exp.* **2016**, 064006 (2016).
20. James, A. J. A., Konik, R. M. & Robinson, N. J. Nonthermal states arising from confinement in one and two dimensions. *Phys. Rev. Lett.* **122**, 130603 (2019).
21. Tan, W. L. et al. Domain-wall confinement and dynamics in a quantum simulator. *Nat. Phys.* **17**, 742–747 (2021).
22. Shiba, H., Ueda, Y., Okunishi, K., Kimura, S. & Kindo, K. Exchange interaction via crystal-field excited states and its importance in $CsCoCl_3$. *J. Phys. Soc. Jpn* **72**, 2326–2333 (2003).
23. Niesen, S. K. et al. Substitution effects on the temperature versus magnetic field phase diagrams of the quasi-one-dimensional effective Ising spin-$\frac{1}{2}$ chain system $BaCo_2V_2O_8$. *Phys. Rev. B* **90**, 104419 (2014).
24. Faddeev, L. & Takhtajan, L. What is the spin of a spin wave? *Phys. Lett. A* **85**, 375–377 (1981).
25. Tennant, D. A., Perring, T. G., Cowley, R. A. & Nagler, S. E. Unbound spinons in the *S*=1/2 antiferromagnetic chain $KCuF_3$. *Phys. Rev. Lett.* **70**, 4003–4006 (1993).
26. Stone, M. B. et al. Extended quantum critical phase in a magnetized spin-$\frac{1}{2}$ antiferromagnetic chain. *Phys. Rev. Lett.* **91**, 037205 (2003).
27. Mourigal, M. et al. Fractional spinon excitations in the quantum Heisenberg antiferromagnetic chain. *Nat. Phys.* **9**, 435–441 (2013).
28. Wu, L. S. et al. Orbital-exchange and fractional quantum number excitations in an f-electron metal, Yb_2Pt_2Pb. *Science* **352**, 1206–1210 (2016).
29. Dmitriev, D. V., Krivnov, V. Y., Ovchinnikov, A. A. & Langari, A. One-dimensional anisotropic Heisenberg model in the transverse magnetic field. *J. Exp. Theor. Phys.* **95**, 538–549 (2002).
30. Halati, C.-M., Wang, Z., Lorenz, T., Kollath, C. & Bernier, J.-S. Repulsively bound magnon excitations of a spin-$\frac{1}{2}$ XXZ chain in a staggered transverse field. *Phys. Rev. B* **108**, 224429 (2023).
31. Daley, A. J., Kollath, C., Schollwöck, U. & Vidal, G. Time-dependent density-matrix renormalization-group using adaptive effective Hilbert spaces. *J. Stat. Mech.* P04005 (2004).
32. White, S. R. & Feiguin, A. E. Real-time evolution using the density matrix renormalization group. *Phys. Rev. Lett.* **93**, 076401 (2004).
33. Schollwöck, U. The density-matrix renormalization group in the age of matrix product states. *Ann. Phys.* **326**, 96–192 (2011).
34. Kimura, S. et al. Novel ordering of an *S* = 1/2 quasi-1D Ising-like antiferromagnet in magnetic field. *Phys. Rev. Lett.* **100**, 057202 (2008).
35. Canévet, E. et al. Field-induced magnetic behavior in quasi-one-dimensional Ising-like antiferromagnet $BaCo_2V_2O_8$: a single-crystal neutron diffraction study. *Phys. Rev. B* **87**, 054408 (2013).
36. Grenier, B. et al. Longitudinal and transverse Zeeman ladders in the Ising-like chain antiferromagnet $BaCo_2V_2O_8$. *Phys. Rev. Lett.* **114**, 017201 (2015).
37. Faure, Q. et al. Tomonaga-Luttinger liquid spin dynamics in the quasi-one-dimensional Ising-like antiferromagnet $BaCo_2V_2O_8$. *Phys. Rev. Lett.* **123**, 027204 (2019).
38. Wang, Z. et al. Quantum critical dynamics of a Heisenberg-Ising chain in a longitudinal field: many-body strings versus fractional excitations. *Phys. Rev. Lett.* **123**, 067202 (2019).
39. Faure, Q. et al. Solitonic excitations in the Ising anisotropic chain $BaCo_2V_2O_8$ under large transverse magnetic field. *Phys. Rev. Res.* **3**, 043227 (2021).
40. Okutani, A. et al. Spin excitations of the *S* = 1/2 one-dimensional Ising-like antiferromagnet $BaCo_2V_2O_8$ in transverse magnetic fields. *J. Phys. Soc. Jpn* **90**, 044704 (2021).

Methods

Sample preparation and characterization

High-quality single crystals of $BaCo_2V_2O_8$ were synthesized by a solid-state reaction using a mixture of $BaCO_3$ (99+%, Merck), Co_3O_4 (99.5%, Alfa Aesar) and V_2O_5 (99.5%, Strem Chemicals) in a 1:2/3:1 molar ratio. A four-mirror image furnace (FZ-T-10000-H-VI-VP, Crystal Systems Inc.) was used for the single-crystal growth by means of the floating-zone technique[14]. For the optical experiments, single crystals were oriented at room temperature using X-ray Laue diffraction. Samples were cut perpendicular to the crystallographic [110] direction with a typical size of $4 \times 4 \times 1\ mm^3$.

Magnetization measurements in pulsed magnetic fields

A bar-shaped $BaCo_2V_2O_8$ single crystal of 2 mm length along the [110] direction and a cross-section of about $1\ mm^2$ was used for the magnetization measurements in a pulsed magnetic field that was applied along the [110] direction, that is, $B \| [110]$. The pulsed field had a rise time of 7 ms and a pulse duration of 20 ms.

The magnetization of $BaCo_2V_2O_8$ obtained at 1.8 K is presented in Extended Data Fig. 1 as a function of the applied transverse magnetic field, $B \| [110]$. The magnetization increases continuously with magnetic field and exhibits a saturation feature at the quantum phase transition of $B_c = 40$ T, as confirmed by the measurements of sound velocity and magnetocaloric effect[15]. Above B_c, a slight increase of the magnetization is ascribed to a Van Vleck paramagnetic contribution with a susceptibility of $0.00895\mu_B$/T (dotted line). As shown by the solid line, the experimental data are very well described by the sum of the Van Vleck contribution (dotted line) and the density matrix renormalization group results for the one-dimensional Heisenberg–Ising model (dashed line) at zero temperature, with the same parameters as for the observed magnetic excitations (see Figs. 1 and 4).

Terahertz spectroscopy in pulsed and static magnetic fields

The high-field electron-spin-resonance spectroscopy in a pulsed magnetic field up to 61 T was performed at Helmholtz-Zentrum Dresden-Rossendorf (HZDR). Absorption spectra of quasi-monochromatic electromagnetic waves were measured as a function of the pulsed magnetic field for frequencies above 1.2 THz using a free-electron laser[41] and below 0.6 THz using VDI microwave sources (Virginia Diodes Inc.) at HZDR. The terahertz broadband transmission measurements were performed in static magnetic fields up to 32 T using a Bitter electromagnet at the High Field Magnet Laboratory in Nijmegen, the Netherlands. Terahertz electromagnetic waves were generated by a mercury lamp and detected by a silicon bolometer. The spectra were recorded using a Fourier-transform spectrometer Bruker IFS 113v. For all of these measurements, the magnetic fields were applied along the crystallographic [110] direction.

Anisotropic *g*-factors and effective magnetic field in $BaCo_2V_2O_8$

Because the CoO_6 octahedra in $BaCo_2V_2O_8$ are slightly distorted with the apical Co–O bonds tilted off the *c* axis (that is, the Ising-like axis; see Fig. 1a), the magnetic local principal axes do not coincide with the crystallographic axes. This results in staggered Landé *g*-factors[13,14]

$$\begin{aligned}
g_j^{xx} &= (g_1\cos^2\theta + g_2\sin^2\theta)\cos^2\left(\frac{\pi}{2}(j-1)\right) + g_3\sin^2\left(\frac{\pi}{2}(j-1)\right),\\
g_j^{xy} &= 0,\\
g_j^{xz} &= (g_2 - g_1)\cos\theta\sin\theta\cos\left(\frac{\pi}{2}(j-1)\right),\\
g_j^{yy} &= (g_1\cos^2\theta + g_2\sin^2\theta)\sin^2\left(\frac{\pi}{2}(j-1)\right) + g_3\cos^2\left(\frac{\pi}{2}(j-1)\right),\\
g_j^{zz} &= g_1\sin^2\theta + g_2\cos^2\theta,\\
g_j^{yz} &= (g_2 - g_1)\cos\theta\sin\theta\sin\left(\frac{\pi}{2}(j-1)\right),
\end{aligned} \tag{2}$$

in which $\theta = 5°$ is the tilt angle from the *c* axis and g_1, g_2 and g_3 are the values of the *g*-tensor along the magnetic principal axes. The *x* coordinate is defined along the crystallographic [110] direction, parallel to the applied magnetic field, whereas the *y* and *z* coordinates are along the [−110] and [001] directions, respectively.

For a transverse magnetic field in the $x \| [110]$ direction, the Zeeman term owing to the effective magnetic field for a single chain in $BaCo_2V_2O_8$ is given by $\mu_B B_x \sum_j (g_j^{xx} S_j^x + g_j^{xz} S_j^z)$, in which $g^{xx}_{1,2,3,4} = (3.72, 2.4, 3.72, 2.4)$ and $g^{xz}_{1,2,3,4} = (0.21, 0, -0.21, 0)$, corresponding to $g_{1,2,3} = 3.7$, 6.1 and 2.4. Owing to the site-dependent anisotropic *g*-factors, the effective magnetic field in the *x* direction has a uniform and a staggered component, corresponding to $g_j^{xx} = g_u^x - (-1)^j g_s^x$, with $g_u^x = 3.06$ and $g_s^x = 0.66$. In the *z* direction, the effective field has a fourfold periodicity, $g_j^{xz} = g^z \sin\left(\frac{\pi}{2}j\right)$, with a small value of $g^z = 0.21$, whose contribution does not play a crucial role for the existence of the repulsively bound states[30]. The parameters obtained are summarized in Extended Data Tables 1 and 2 and compared with the reported values in the literature. Although the values of J, Δ and g_u^x are consistent with the reported values[13,16,38,40,42], the value of g_s^x corresponding to the staggered field is relatively small and was neglected in the literature. By contrast, we have shown the importance of a finite staggered field, which is responsible for the splitting of the low-lying single-magnon band (see Extended Data Fig. 2) and enhances the dynamical response of the repulsively bound magnons (see Extended Data Figs. 3 and 4). These parameters are further constrained by the field dependence of the magnetization (see Extended Data Fig. 1).

Numerical simulations using the matrix product state technique

We investigate theoretically the excitations observed experimentally by computing the dynamical spin structure factor, $\mathcal{S}(q,\omega)$. In linear response, the definition we use is given by

$$\begin{aligned}
\mathcal{S}(q,\omega) = \sum_{l=L/2-1}^{L/2+2} &[\,|(gS)_l^{zz}(q,\omega)|^2 + |(gS)_l^{yy}(q,\omega)|^2 + |(gS)_l^{zy}(q,\omega)|^2\\
&+ |(gS)_l^{yz}(q,\omega)|^2\,].
\end{aligned} \tag{3}$$

Because the terahertz field is unpolarized and perpendicular to the applied external field, equation (3) contains the relevant transverse components, which are defined by

$$(gS)_l^{\alpha\beta}(q,\omega) = \frac{1}{\sqrt{L}}\int_0^\infty \sum_{j=1}^{L} e^{i(\omega t - qj)}\mathcal{G}_j^\alpha \mathcal{G}_l^\beta S_{j,l}^{\alpha\beta}(t)\,dt \tag{4}$$

with $\alpha, \beta \in \{x, y, z\}$, $\mathcal{G}_l^x = g_l^{zx}$, $\mathcal{G}_l^y = g_l^{yy} + g_l^{zy}$, $\mathcal{G}_l^z = g_l^{zz} + g_l^{yz}$ and the two-point correlation functions $S_{j,l}^{\alpha\beta}(t) = \langle 0|\ S_j^\alpha(t) S_l^\beta\ |0\rangle$ for the spin operators S_j^α and S_j^β. The index l enumerates the four Co^{2+} spin sites in the central unit cell. The ground state, denoted by $|0\rangle$, and the time-dependent correlations are computed numerically using matrix product state algorithms (see below).

The numerical simulations performed in this work for the one-dimensional model, equation (1), are based on the matrix product states techniques[31–33]. This method is variational in the space of matrix product states characterized by a certain matrix dimension, called the bond dimension. The loss of accuracy in the representation of the wavefunction in an approximation state is quantified by the truncation error. The ground state $|0\rangle$ is obtained using a finite-size density matrix renormalization group algorithm[33] in the matrix product state representation implemented using the ITensor library[43]. The convergence is ensured by a maximal bond dimension up to 300, for which the truncation error is at most 10^{-12}. The two-point correlations are computed numerically using the time-dependent matrix product state method[31–33]. We considered systems of $L = 124$ sites and bond dimensions up to 300. This ensures that, at the final time $tJ/\hbar = 110$, the truncation error is

$\leq 10^{-7}$ (or $\leq 10^{-10}$ above the phase transition). The time step is $\delta t J/\hbar = 0.05$ and the measurements were performed every fourth time step. To minimize the numerical artefacts arising as a result of the use of open boundary conditions, we applied a Gaussian filter, $f(j) = e^{-4\left(1-\frac{2j}{L-1}\right)^2}$, to the dynamic correlations before performing the numerical Fourier transform. Here j labels the sites.

Effects of the effective staggered magnetic field

We have emphasized that the staggered magnetic field plays a very important role in the visibility and detection of the multi-magnon bound states. This can be systematically shown by performing numerically exact calculations with the matrix product state technique for various values of g_s^x, which is responsible for the staggered field.

We consider three different regimes: above the phase transition, $B > B_c$ (see Extended Data Fig. 2), at the phase transition $B \approx B_c$ (see Extended Data Fig. 3) and below the phase transition (but still at large magnetic field), $0 \ll B < B_c$ (see Extended Data Fig. 4). The values of the other parameters are the same as for the results of the main text, $J = 2.82$ meV, $\Delta = 1.92$, $g_u^x = 3.06$ and $L = 124$, except the fourfold field, which is absent ($g^z = 0$). We can show that the small value of $g^z = 0.21$ does not influence the characteristic features of the repulsively bound magnon states (see ref. 30).

For $B > B_c$, the spins are polarized along the field direction. Without a staggered field, $g_s^x = 0$, the excitations are characterized by the dynamics of single magnons moving through the chain. This determines a single cosine-shaped band in the structure factor (see Extended Data Fig. 2a; denoted by M). If the staggering becomes finite, $g_s^x > 0$, this band is split into two with a gap. This is because a propagating single magnon around the lattice experiences site-dependent lower or higher effective magnetic field. This can also be seen from the fact that the gap increases with increasing staggered field (see Extended Data Fig. 2b–d for $g_s^x \in \{0.31, 0.66, 0.94\}$). We mention that the results in Extended Data Fig. 2c correspond to the same staggering, $g_s^x = 0.66$, as for the parameters considered in Fig. 4 describing $BaCo_2V_2O_8$.

In the case of a magnetic field close to the critical value, $B \approx B_c$, we can clearly distinguish the two-magnon bound states features at the experimental value $g_s^x = 0.66$ (Extended Data Fig. 3c, see also Fig. 4). If we increase the staggering, the spectral weight of the repulsively bound two-magnon excitations becomes even more prominent (Extended Data Fig. 3d), whereas at lower and vanishing staggering, the spectral weight strongly decreases and becomes hardly discernible (see Extended Data Fig. 3a,b).

Similarly, for magnetic field below B_c but still large, that is, $0 \ll B < B_c$, starting from the experimental value $g_s^x = 0.66$ (Extended Data Fig. 4c), an increase or decrease of the staggered field will enhance or reduce, respectively, the spectral weight of the repulsively bound two-magnon (denoted by D) and three-magnon (denoted by T) states. It is important to note that, even without the staggered field, the repulsively bound multi-magnon states are present in the model, owing to the interplay of the antiferromagnetic interactions and strong magnetic fields[30]. However, their presence in the dynamical structure factors as well-defined features with a spectral weight large enough to be detected experimentally is because of the presence of a strong staggering of the effective magnetic field, as in the case of $BaCo_2V_2O_8$.

Guiding principles for identifying repulsively bound magnons

Our study reveals the following guiding principles for identifying repulsively bound magnons. First, spin interactions should be dominated by antiferromagnetic intrachain exchange with negligible interchain couplings, enhancing one-dimensional quantum fluctuations. Second, the intrachain interaction should be sufficiently stronger than thermal energy, such that the spin dynamics is governed by quantum-mechanical effects. A strong intrachain interaction also corresponds to a large quantum critical field; therefore the three-dimensional order stabilized by the interchain couplings is already suppressed well below the one-dimensional quantum critical point. Third, to avoid a fast decay of the repulsively bound magnons, dissipation channels (for example, a direct coupling with phonons or other degrees of freedom) should be minimized as much as possible. Last but not least, the staggered magnetic field in $BaCo_2V_2O_8$ increases the separation of the repulsively bound magnons from the lower-energy excitations and also enhances their dynamical responses, facilitating the experimental identification.

Data availability

All data needed to evaluate the conclusions in the paper are included in this paper. Further data that support the plots and other analysis in this work are available from the corresponding author on request. The theoretical simulations data are available at https://doi.org/10.5281/zenodo.11521387 (ref. 44).

41. Zvyagin, S. A. et al. Terahertz-range free-electron laser electron spin resonance spectroscopy: techniques and applications in high magnetic fields. *Rev. Sci. Instrum.* **80**, 073102 (2009).
42. Wang, X. et al. Spin dynamics of the E_8 particles. Preprint at https://doi.org/10.48550/arXiv.2308.00249 (2023).
43. Fishman, M., White, S. R. & Stoudenmire, E. M. The ITensor software library for tensor network calculations. *SciPost Phys. Codebases* 4 https://scipost.org/10.21468/SciPostPhysCodeb.4 (2022).
44. Halati, C.-M., Wang, Z., Kollath, C. & Bernier, J.-S. Theoretical simulations data for "Experimental observation of repulsively bound magnons". *Zenodo* https://doi.org/10.5281/zenodo.11521387 (2024).

Acknowledgements We thank M. Garst, T. Giamarchi, S. Wolff, J. Wu and H. Zou for helpful discussions. We acknowledge support by the European Research Council (ERC) under the Horizon 2020 research and innovation programme, grant agreement no. 950560 (DynaQuanta), by the Natural Sciences and Engineering Research Council of Canada (NSERC) (funding reference nos. RGPIN-2021-04338 and DGECR-2021-00359) and by the Swiss National Science Foundation under Division II grants 200020-188687 and 200020-219400. This research was supported in part by the National Science Foundation under grant nos. NSF PHY-1748958 and PHY-2309135. We acknowledge funding from the Deutsche Forschungsgemeinschaft (DFG, German Research Foundation) under project number 107745057 - TRR 180 (F5), project number 277146847 - CRC 1238 (A02, B01, B05, C05), project number 277625399 - TRR 185 (B4), project number 247310070 - SFB 1143, project number 511713970 - CRC 1639, project number 390858490 - EXC 2147 Cluster of Excellence Complexity and Topology in Quantum Matter (CT.QMAT) and project number 390534769 - EXC 2004/1 Cluster of Excellence Matter and Light for Quantum Computing (ML4Q). We also acknowledge the support of the HFML-RU/FOM and the HLD at Helmholtz-Zentrum Dresden-Rossendorf (HZDR), members of the European Magnetic Field Laboratory (EMFL). Parts of this research were carried out at ELBE at the HZDR, a member of the Helmholtz Association.

Author contributions Z.W. conceived the experiment and coordinated the project. C.-M.H., J.-S.B. and C.K. performed the theoretical analysis. Z.W., A.P., J.M.K. and S.Z. carried out the spectroscopic measurements. D.I.G., T.L. and Z.W. performed the magnetization measurements. S.N., O.B. and T.L. prepared and characterized the single crystals. Z.W., C.-M.H., J.-S.B. and C.K. analysed the data and interpreted the results. Z.W., C.-M.H., J.-S.B. and C.K. wrote the manuscript, with input from T.L. and A.L. All authors commented on the manuscript.

Competing interests The authors declare no competing interests.

Additional information

Correspondence and requests for materials should be addressed to Zhe Wang.

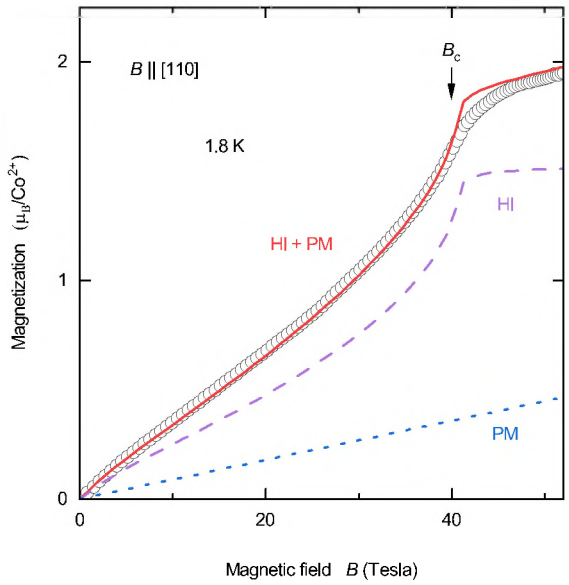

Extended Data Fig. 1 | Magnetization of $BaCo_2V_2O_8$ as a function of the applied magnetic field along the crystallographic [110] direction[15], that is, B||[110]. The solid line shows the theoretical result, as a sum of a paramagnetic (PM) Van Vleck contribution (dotted line) and the contribution of the one-dimensional Heisenberg–Ising (HI) model in equation (1) (dashed line).

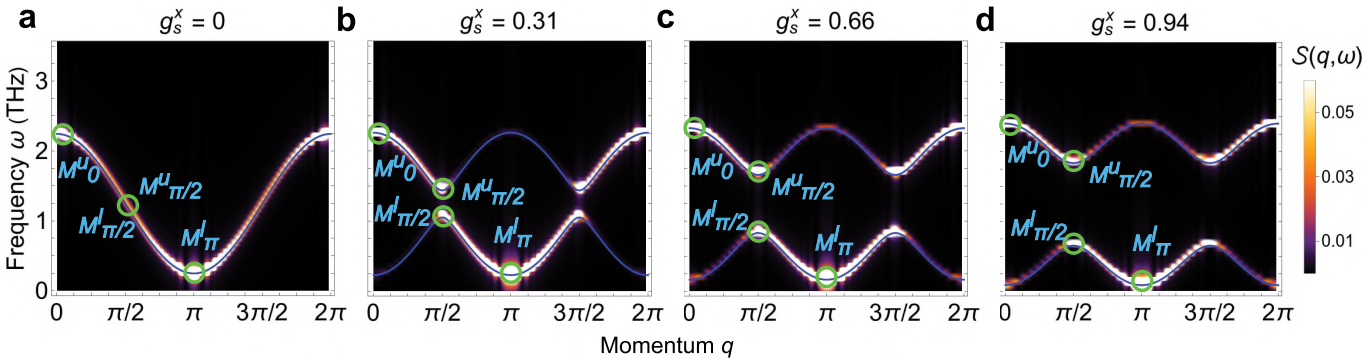

Extended Data Fig. 2 | Dynamical spin structure factor $\mathcal{S}(q,\omega)$ as a function of momentum q and frequency ω (see equation (3)) at an applied field of $B = 45\,\mathrm{T} > B_c$ for various values of g_s^x corresponding to different effective staggering of the magnetic field. a, Without a staggered field (that is, $g_s^x = 0$), the spin dynamics is characterized by a single cosine-shaped band of unbound-magnon excitations, labelled as M. **b**–**d**, With a finite staggered field (that is, $g_s^x = 0.31$, 0.66 and 0.94, respectively), this band is split into two bands, separated by a gap. The gap increases with increasing staggered field. The data in **c** correspond to the experimental value of the staggering in $BaCo_2V_2O_8$ (see Fig. 4c). The blue lines are analytical results for the one-magnon excitations[30].

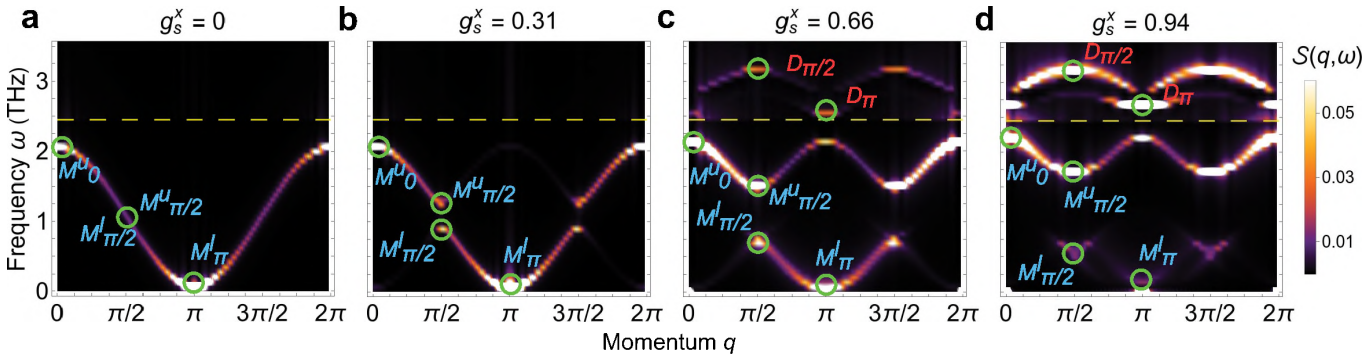

Extended Data Fig. 3 | Dynamical spin structure factor $\mathcal{S}(q,\omega)$ as a function of momentum q and frequency ω (see equation (3)) at an applied field of $B = 40.3\,\mathrm{T} \approx B_c$ for various values of g_s^x corresponding to different effective staggering of the magnetic field. Above the dashed line, the spectral weight of the repulsively bound two-magnon states (labelled as D) is multiplied by a factor of 10. The data in **c** correspond to the experimental value of the staggering for $BaCo_2V_2O_8$ (see Fig. 4b).

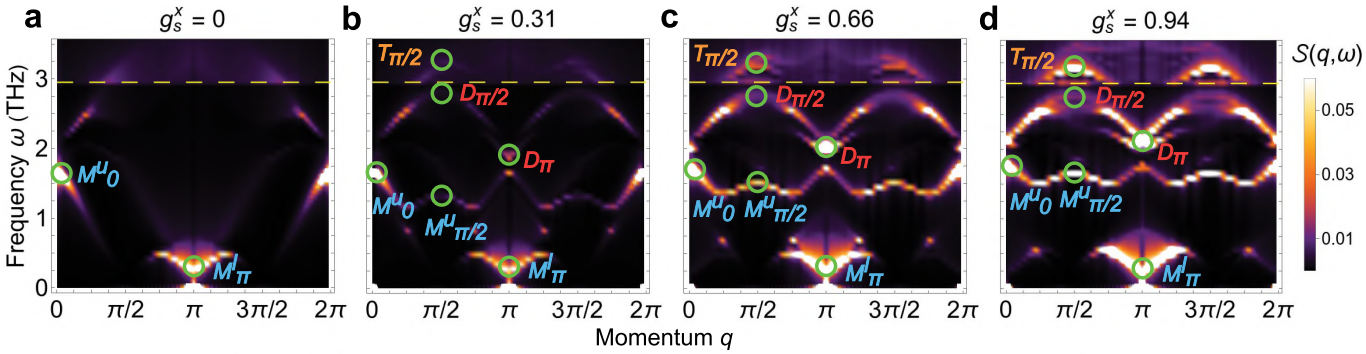

Extended Data Fig. 4 | Dynamical spin structure factor $\mathcal{S}(q,\omega)$ as a function of momentum q and frequency ω (see equation (3)) at an applied field of $B = 30$ T (that is, $0 \ll B < B_c$) for various values of g_s^x corresponding to different effective staggering of the magnetic field. a, Without a staggered field (that is, $g_s^x = 0$), the high-energy features above the unbound-magnon excitation band are hard to identify. However, with increasing staggered field for $g_s^x = 0.31$ (**b**), for $g_s^x = 0.66$ (**c**) and for $g_s^x = 0.94$ (**d**), the spectral weight of the features of repulsively bound two-magnon and three-magnon excitations (labelled as D and T, respectively) can be clearly identified and is continuously enhanced. Above the dashed line, the spectral weight of the repulsively bound three-magnon states is multiplied by a factor of 10. The data in **c** correspond to the experimental value of the staggering for $BaCo_2V_2O_8$ (see Fig. 4a).

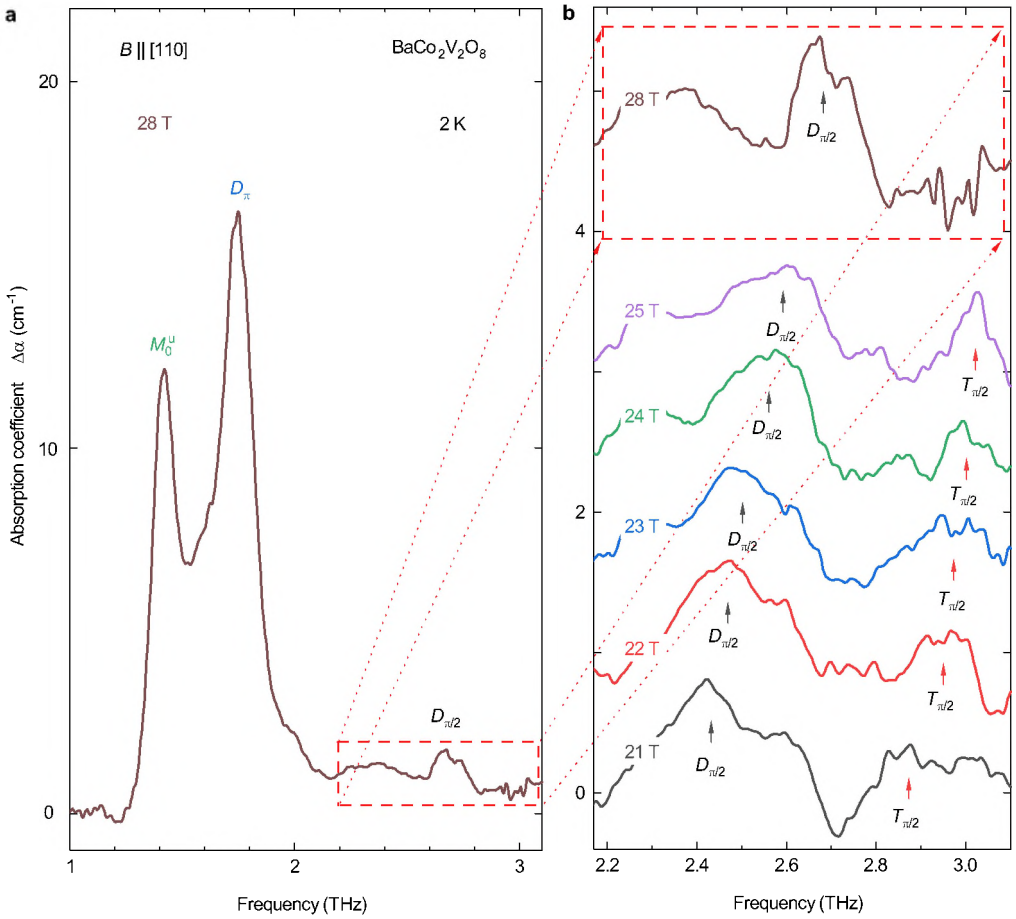

Extended Data Fig. 5 | Absorption coefficient measured in static magnetic fields. a, The spectrum at 28 T with the single-magnon M_0^u and the repulsively bound two-magnon D_π and $D_{\pi/2}$ modes (see also Fig. 3). **b**, Zoom-in of the high-frequency spectral range corresponding to the $D_{\pi/2}$ and the repulsively bound three-magnon $T_{\pi/2}$ modes (as indicated by the arrows) measured at various fields.

Extended Data Table 1 | The parameters *J* and Δ

	Ref.[13]	Ref.[16]	Ref.[38]	Ref. [40]	Ref.[42]	This work
J (meV)	2.58	3.07	2.6	2.58	2.67	2.82
Δ	2.17	1.89	2.17	2.17	2.17	1.92

Data from refs. 13,16,38,40,42.

Extended Data Table 2 | The parameters of the *g*-values g_u^x, g_s^x and g_z

	Ref.[13]	Ref. [40]	This work
g_u^x	2.95	2.95	3.06
g_s^x	0	0	0.66
g_z	0.41	0.41	0.21

Data from refs. 13,40.